

Article

Geochemical Characteristics of Iron in a Sediment Core at 63°40' E, Eastern Southwest Indian Ridge: Implications on Regional Hydrothermal Activities and Source Origin

P. Linsy, L. Surya Prakash, Parijat Roy, Muhammad Shuhail  and P. John Kurian * 

National Centre for Polar and Ocean Research, Ministry of Earth Sciences, Vasco-da-Gama 403804, Goa, India

* Correspondence: john@ncpor.res.in

Abstract: Iron is a limiting nutrient in the marine biogeochemical cycle, and hydrothermal processes at mid-ocean ridges are well-known as one of its sources to the water column. However, a major portion of the hydrothermal iron is precipitated near the source and plays an essential role in oceanic elemental cycling. Here, we carried out a detailed study on the geochemical characteristics of Fe, using a sequential chemical extraction protocol, in a short sediment core collected from the eastern Southwest Indian Ridge (SWIR) to understand the iron association in individual mineral phases. Major and trace and rare-earth element concentrations, positive europium anomaly, and rare-earth fractionation show that the source components in the sediment core are composed of biogenic, local mafic, ultramafic, and hydrothermal origin. Solid-phase Fe speciation results indicate that >60% of Fe is associated with the Fe-oxides phase and indicate the hydrothermal plume particulates settled from the water column. A relatively low concentration of Fe associated with the pyrite and silicate (Fe_{Res}) phase suggests an erosion of sulphide and silicate minerals from the nearby vent field. The down-core variation reflects the transformation of primary ferrihydrite to more stable oxide mineral goethite/hematite and, to some extent, the formation of silicate minerals.

Keywords: Fe geochemistry; hydrothermal; SWIR; deep-sea sediments; iron speciation



Citation: Linsy, P.; Surya Prakash, L.; Roy, P.; Shuhail, M.; Kurian, P.J. Geochemical Characteristics of Iron in a Sediment Core at 63°40' E, Eastern Southwest Indian Ridge: Implications on Regional Hydrothermal Activities and Source Origin. *Minerals* **2023**, *13*, 209. <https://doi.org/10.3390/min13020209>

Academic Editors: Francisco J. González, A. Filipa A. Marques and Blanca Rincón-Tomás

Received: 21 November 2022

Revised: 21 January 2023

Accepted: 23 January 2023

Published: 31 January 2023



Copyright: © 2023 by the authors. Licensee MDPI, Basel, Switzerland. This article is an open access article distributed under the terms and conditions of the Creative Commons Attribution (CC BY) license (<https://creativecommons.org/licenses/by/4.0/>).

1. Introduction

Seafloor hydrothermal activity is one of the fundamental processes that control the exchange of heat and chemical fluxes between seawater and ocean rocks [1–3] and contributes ~12%–22% of the dissolved Fe budget to the deep ocean [4,5]. Mixing vent fluid with oxic bottom water leads to the precipitation of Fe-rich sulphides and oxyhydroxides [6]. Iron sulphide minerals precipitate rapidly, while hydrous oxide continues to precipitate for some time in the neutrally buoyant plume [6–8].

The fluxes of Fe into and out of the ocean are important since it has a direct impact on the oceanic primary productivity, where iron is an essential bio-element and frequently acts as a limiting micronutrient in the ocean. In sediments, iron distributes among different mineral phases and shows different geochemical behaviour. Thus, the geochemical characteristics of Fe in hydrothermally altered sediments are important for understanding the contribution of hydrothermal sediments to the oceanic Fe inventory. Sequential chemical extraction of Fe is a potential tool for understanding the distribution of Fe among different mineral phases and their post-depositional changes in sediments.

Hydrothermally precipitated Fe-oxyhydroxides are effective sinks of trace and rare-earth elements in the ocean [9]. The diagenetic alteration of Fe may lead to the release of these elements into the seawater. Thus, hydrothermal processes strongly influence the trace element budget of the ocean [10]. However, most of the studies on Fe geochemistry and its role in trace metal chemistry focus on hydrothermal plumes [10–12], with very few studies concentrating on hydrothermal sediments.

The past geochemical investigations on surface sediments and ferromanganese encrustations of ultraslow spreading Southwest Indian Ridge (SWIR) have mainly focused on understanding the hydrothermal activity in the region [13–21]. However, studies on the geochemical characteristics of iron and its distribution among major mineral phases in sediments to understand the role of Fe on the geochemistry of trace elements are very limited in the SWIR. Therefore, in order to understand the source characteristics of sediments in the SWIR, we studied a short sediment core recovered from the deepest part of a Non-Transform Discontinuity (NTD) ($63^{\circ}39' E$) close to the Tianzuo vent field [22–24]. The primary objective of this study is to determine the geochemical characteristics of Fe in sediments and to understand the distribution of Fe among chemically separable mineral phases and their post-depositional transformation.

2. Study Area and Sampling

The SWIR is a slow to ultraslow spreading mid-oceanic ridge that separates Antarctic and African plates and extends from the Rodrigues Triple Junction to Bouvet Triple Junction over a length of 7700 km [25,26]. Earlier studies have shown that the seafloor generation over the SWIR has both magmatic and amagmatic sections due to its magma-poor mode of spreading [27]. The eastern part of the SWIR, between Melville FZ and Rodrigues Triple Junction (RTJ), trends in the NNE-SSW direction (Figure 1). This part of the SWIR is segmented by several NTDs and is devoid of fracture zones. Previous studies in this area have shown that the seafloor is mainly covered by basalt; however, peridotite, gabbro, and diabase have also been reported in some areas [18,28,29]. Most of the sediments in this area are mainly composed of calcareous skeletons with low content of detrital materials and pelagic clays [30].

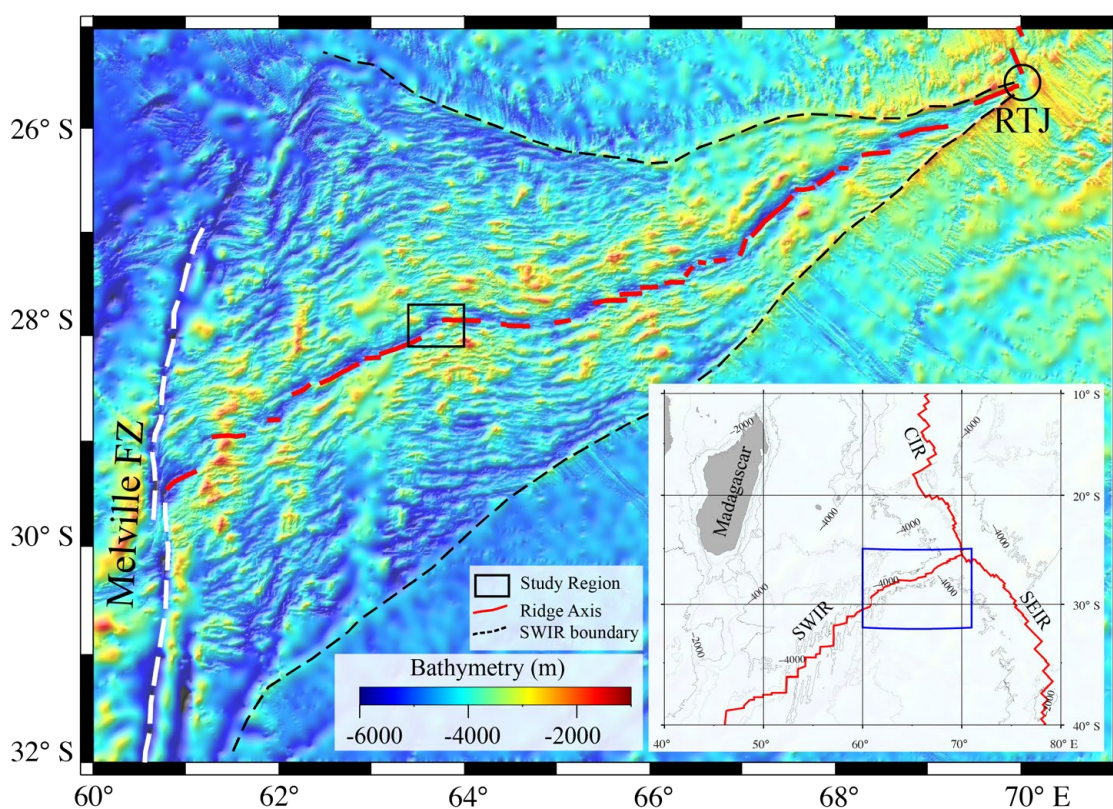


Figure 1. Colour-coded GEBCO bathymetric map of the SWIR between the Melville FZ and Rodrigues Triple Junction (RTJ). The white dashed line represents the Melville Fracture Zone. The SWIR seafloor boundary is marked with black dashes. CIR: Central Indian Ridge; SWIR: Southwest Indian Ridge; SEIR: Southeast Indian Ridge.

A box core (BC-10) of length 40 cm was retrieved onboard RV MGS Sagar (Cruise # MGS-25) from the deepest part of the 63°40' NTD (27°56'54" S and 63°39'25" E) at a water depth of 5638 m (Figure 2). Three hydrothermal field sites were reported in the proximity of the BC-10 station (Figure 2). The closest field, Tianzuo, located at a distance of ~12.5 km towards the west, is situated on a dome-shaped structure and hosted by ultramafic rocks [23]. This structure has evolved over the oceanic detachment fault system forming as oceanic core complexes, exposing the mantle-derived rocks. Hydrothermal activities in this field were supposed to be controlled by a detachment fault and the recovered ultramafic rocks show high serpentinization [23]. Two closely spaced vent fields on segment 11, the Tiancheng [24] and Mt. Jourdanne [22], are at a distance of ~32 km from our sampling station. The Mt. Jourdanne field is hosted by basaltic hosted rocks and is the earliest reported vent field from the SWIR [31]. The Tiancheng field is a low-temperature diffuse flow hydrothermal field hosted by basaltic rocks [23].

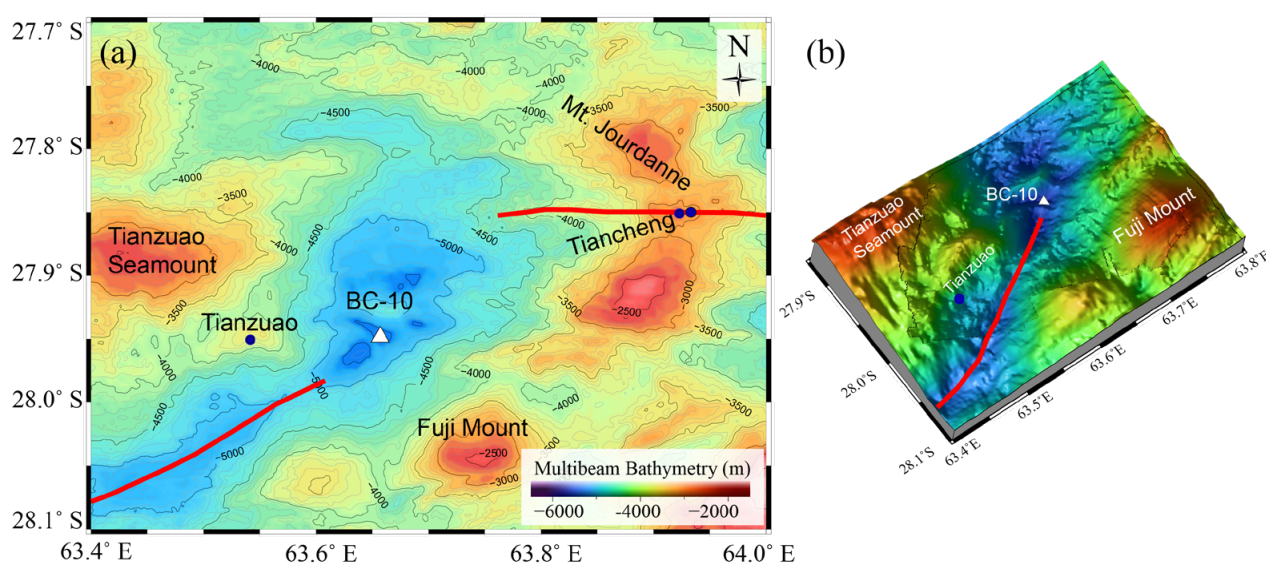


Figure 2. Bathymetric maps showing the location of the BC-10 sampling station. (a) Colour-coded bathymetric map with 100 m contours highlighting the topographic features surrounding the sampling location. The ridge segments are shown as red lines. The reported hydrothermal fields are marked with blue circles. (b) A 3D perspective map of the study area was prepared using the multibeam data collected during the MGS-25 expedition.

3. Materials and Methods

The core was sub-sampled at 1 cm intervals onboard and stored at -20°C for further biogeochemical analyses. Sub-sampled sediment samples were freeze-dried and ground by using an agate mortar and pestle. The coarse fractions of a few representative sediment samples were separated by soaking sediments in 10% Na-hexametaphosphate and later wet-sieved through an ASTM mesh of $>63\ \mu\text{m}$. The coarse fractions of the selected samples were examined for morphological features using a scanning electron microscope (SEM-JEOL JSM 6360 LV) at the National Centre for Polar and Ocean Research Goa, India. Energy Dispersive Spectroscopy (EDS- model: OXFORD INCA 150) was used for the determination of the elemental composition of grains. Bulk mineralogy of the sediments was determined using a Rigaku (Ultima IV) X-Ray diffractometer with Cu-K α 1 radiation and Ni filter over a 2θ range between 3 and 80° at the CSIR-National Institute of Oceanography, Goa.

Finely-ground bulk sediment samples were digested with an acid mixture of HF, HNO $_3$, and HClO $_4$ at a ratio of 7:3:1, and prepared the final solutions in a 4% HNO $_3$ medium. Major elements were determined by using inductively coupled plasma-optical emission spectroscopy (ICP-OES) at the Palaeothermometry lab. Trace and rare-earth elements were measured using inductively coupled plasma mass spectrometry (ICP-MS;

Agilent 7700X). The standard reference materials, JMS-1, JMS-2 (Geological Survey of Japan), and SGR-1b (Green River Shale from United States of Geological Survey), were used to monitor the accuracy of the analysis, and the error was within $\pm 7\%$. The analytical precision calculated from the duplicate measurement was generally $<5\%$. The total inorganic carbon content of the samples was determined using a CO_2 coulometer (UIC model 5030). The accuracy of the analysis was determined using pure calcium carbonate as the standard, and the error was within $\pm 4\%$.

The R programming language was utilized to perform correlation analysis and hierarchical clustering on the bulk sediment analysis data. The criteria for group formation were based on a 90% significance threshold of the correlation coefficient ($r = 0.27$; $n = 40$; $p = 0.09$). Elements within the same group exhibit statistically significant correlation among themselves, as determined by the dissimilarity measure $1-r$, where ' r ' represents the Pearson correlation coefficient.

The sequential chemical extraction method developed by Poulton and Canfield [32] was adopted for the separation of iron associated with different mineral phases, namely (i) carbonate and acid volatile sulphide ($\text{Fe}_{\text{Acetate}}$), (ii) easily reducible oxides ($\text{Fe}_{\text{HA-HCl}}$), (iii) reducible oxides ($\text{Fe}_{\text{Dithionite}}$), (iv) recalcitrant oxides ($\text{Fe}_{\text{Oxalate}}$), (v) poorly reactive sheet silicates (Fe_{HCl}), and (vi) residual Fe (Fe_{Res} —Fe associated with un-reactive silicates and pyrite). The efficiency of the above-mentioned method [32], chemical separation of Fe-phases in natural sediments, was argued for its overestimation of the $\text{Fe}_{\text{Oxalate}}$ phase (specially targeted for magnetite minerals) [33]. However, recent studies of [34] in natural sediments have clearly shown that the Fe oxalate phase is less than 1% after the physical separation of magnetic minerals (magnetite) and concluded that operationally defined oxalate fraction is highly selective for magnetite and yields precise quantitative information on its abundance.

Ten samples were selected for the sequential chemical extraction study. All the extractions were performed at room temperature, and before each step, the residue was repeatedly washed with ultrapure water. Detailed steps of the extractions are shown in Table 1. The Fe, Mn, Mg, and Al concentrations in each phase were determined by using inductively coupled plasma-optical emission spectroscopy (ICP-OES) at the Palaeothermometry lab, National Centre for Polar and Ocean Research. The data quality and reliability of the method were assessed by standard reference materials and duplicate measurements of samples. The recovery of extractions was checked by measuring the total content of the element in a separate aliquot of the sample, and recovery for Fe, Mn, Al, and Mg are as follows: 92%–98%, 85%–97%, 89%–103%, and 88%–91%.

Table 1. The sequential chemical extraction protocol of Fe in sediments adopted from Poulton and Canfield [32].

Extraction	Target Phase	Term
1×10 mL 1 M CH_3COONa (pH—4.5)	Easily exchangeable/loosely sorbed Fe, Carbonate Iron, and acid volatile iron sulphide	$\text{Fe}_{\text{Acetate}}$
1×10 mL 1 M hydroxylamine-HCl (in 25% <i>v/v</i> acetic acid)	Ferrihydrite and lepidocrocite	$\text{Fe}_{\text{HA-HCl}}$
1×10 mL sodium dithionite (50 g/L) (pH—4.8)	Goethite, akaganeite, and hematite	$\text{Fe}_{\text{Dithionite}}$
1×10 mL 0.2 M Ammonium oxalate/0.17 M oxalic acid Boil with 12N HCl	Magnetite	$\text{Fe}_{\text{Oxalate}}$
Digestion with concentrated HF, HNO_3 , and HClO_4 mixture and final dissolution in 2% (<i>v/v</i>) HNO_3 .	Poorly reactive sheet silicate Fe Un-reactive silicate Fe and Pyrite Fe	Fe_{HCl} Fe_{Res}

4. Results

4.1. Lithology and Mineralogy of the Sediment Core

The SEM analysis of the sediment core showed an abundance of siliceous microfossils and glass shards. The energy dispersive spectrum analysis of the same confirms the presence of glass shards and Fe-Mn-Si oxides in the samples (Figure 3).

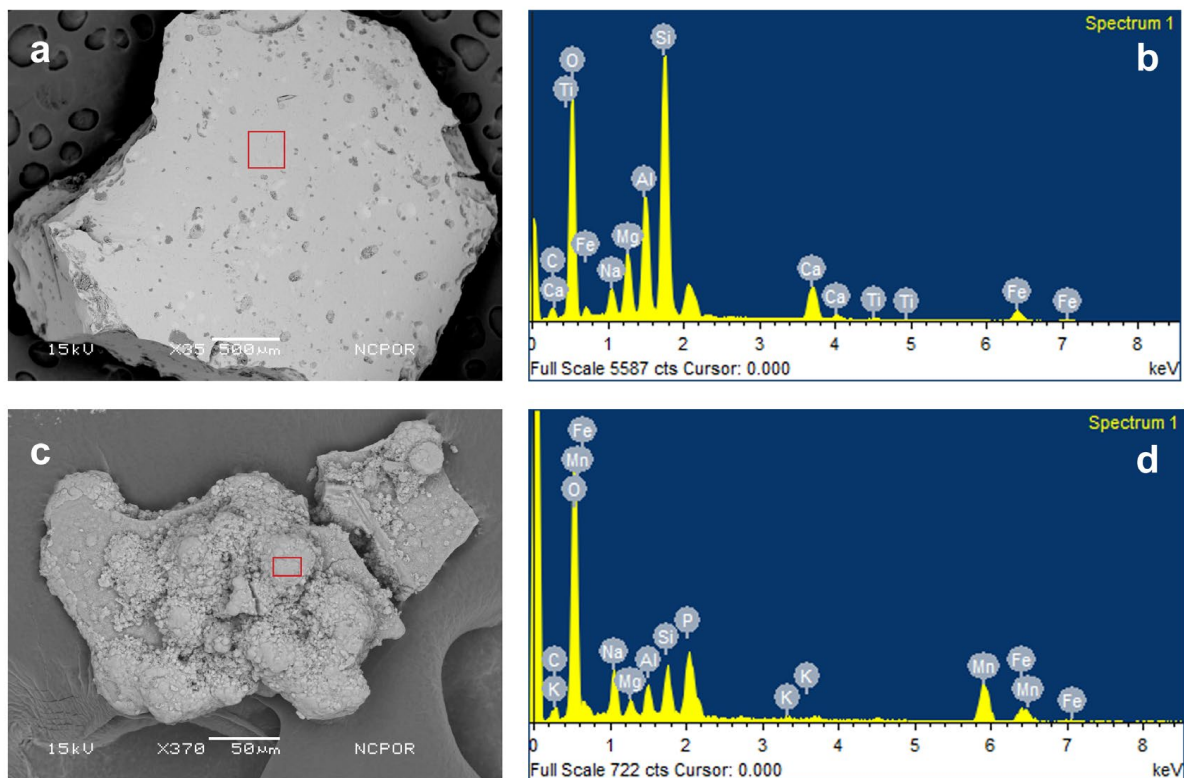


Figure 3. SEM image and EDS spectra of sample. (a) SEM image of glass shards obtained from the core, (b) EDS spectra of the glass shards, (c) SEM image of Fe-Mn-Si oxides, and (d) EDS spectra of Fe-Mn-Si oxides.

The x-ray diffractogram (XRD) studies on selected samples from the core are carried out for mineralogical composition and show nearly consistent and uniform peaks. The results reveal the presence of hematite, goethite, magnetite, nontronite, pyrite, halite, kaolinite, chlorite, and illite in the sediment core (Figure 4). A slight bulge emerges under the baseline of the sample near $d = 2.62 \text{ \AA}$ and 1.51 \AA (2θ centers were approximately 34.5° and 61.3°), indicating the presence of poorly reactive 2-line crystalline ferrihydrite (Figure 4) [35,36]. Another weak hump at about 4.08 \AA (2θ between $17\text{--}26^\circ$) suggests the presence of amorphous opal in this core [35]. The results also indicate the presence of phillipsite in the sediment core, which is also evidenced by the peaks for Si-Al-Na and Ca/K in the EDS analyses. Phillipsite is a zeolite group of minerals formed by the alteration of volcanogenic glass [37]. The abundance of volcanogenic glasses and the high Si content in the sediments support the formation of phillipsite.

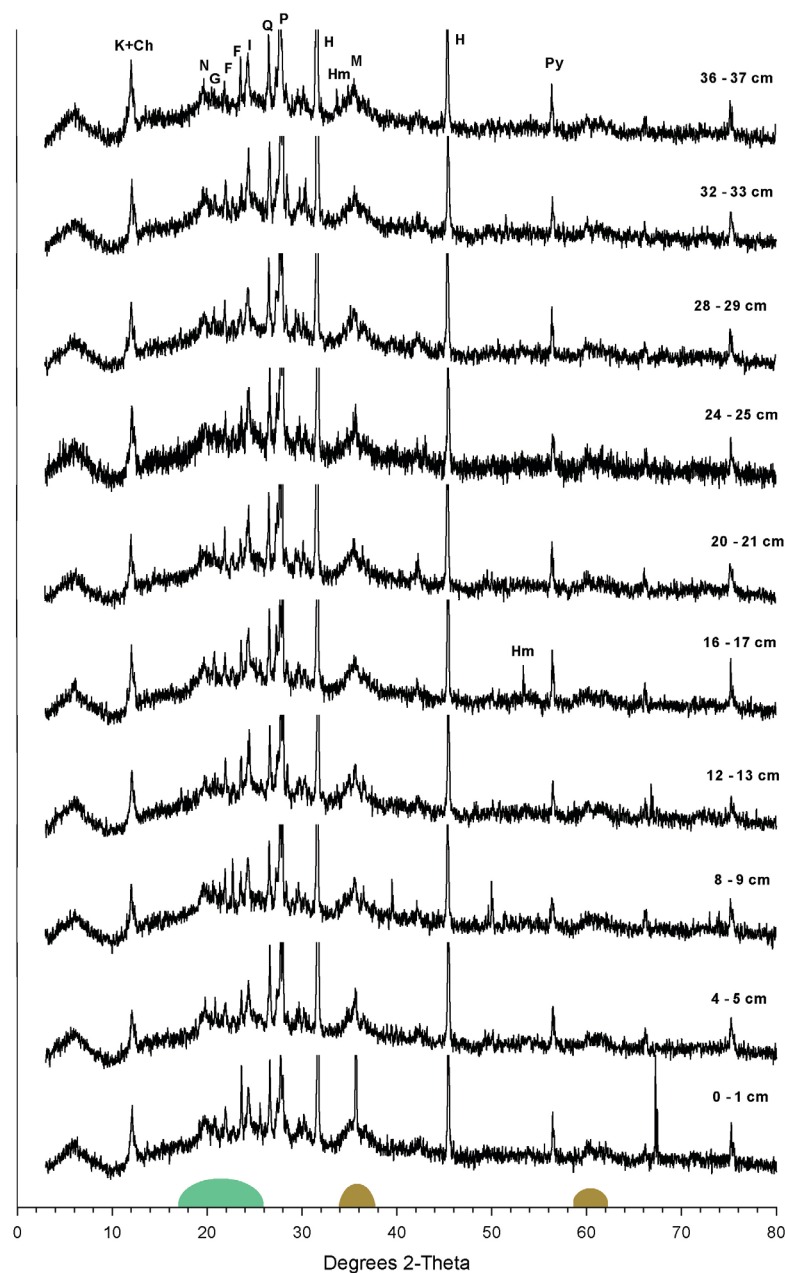


Figure 4. XRD pattern of the sediment core, K—kaolinite, Ch—chlorite, N—nontronite, G—goethite, F—feldspar, I—illite, Q—quartz, P—phillipsite, H—halite, Hm—hematite, M—magnetite, and Py—pyrite. Green shaded area represents amorphous opal, and brown represents poorly crystallized Fe-oxyhydroxide.

4.2. Bulk Geochemistry of Sediments

The results of the bulk geochemical analysis of the sediment core are shown in Figure 5. It is very interesting to note the absence of any calcareous ooze throughout the core, and it contains no carbonate since the sediment core was recovered from a water depth of 5638 m, much below the calcium carbonate compensation depth (4600–4800 m) of the study area [38]. TIC analysis shows nearly zero value, confirming the absence of carbonate in sediment. The iron concentration is relatively enriched throughout the core, with an average value of 7.32 wt.% (Figure 5). The Mn concentration varies from 0.73 to 0.83 wt.% (Table S1). Al, Mg, and Ti concentrations are 5.9–6.8, 4.4–5.24, and 0.42–0.45 wt.%, with an average of 6.49, 4.64, and 0.46 wt.%, respectively.

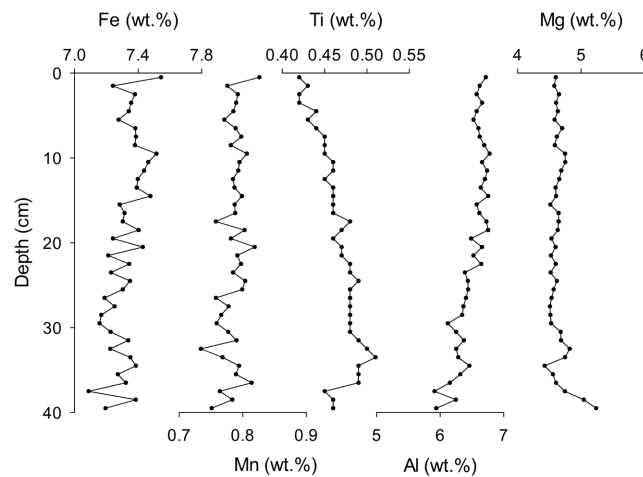


Figure 5. Down-core variations of Fe, Mn, Ti, Al, and Mg measured in the sediment core BC-10.

The copper content of the sediment core ranges from 234 to 267 $\mu\text{g/g}$ (average—247.5 $\mu\text{g/g}$) and is relatively low compared with near-vent metalliferous sediments, which show average values of 17.3% [9]. The concentration of Zn, Pb, Ni, and Cr are 111–195, 25–35, 324–429, and 267–371 $\mu\text{g/g}$, with an average of 142, 31, 352, and 293 $\mu\text{g/g}$, respectively (Table S1). Trace metal concentrations of the studied core are relatively higher than the background sediments from the SWIR [20].

Rare-earth element (REE) concentrations were normalized with Post Archean Australian Shale values (PAAS). PAAS normalized REE patterns (Figure 6) of the bulk sediments exhibit a positive Eu anomaly (Eu/Eu^* ratios vary from 1.2 to 1.4) and no Ce anomaly compared with the other lanthanides (Table S2). The REE pattern of the BC-10 sediment core shows lighter REE (LREE) depletion and heavier REE (HREE) enrichment throughout the core. REE patterns characterized by LREE depletion, HREE enrichment, and positive Eu anomaly are similar to the REE pattern of metalliferous sediments from the Central Indian Basin [39].

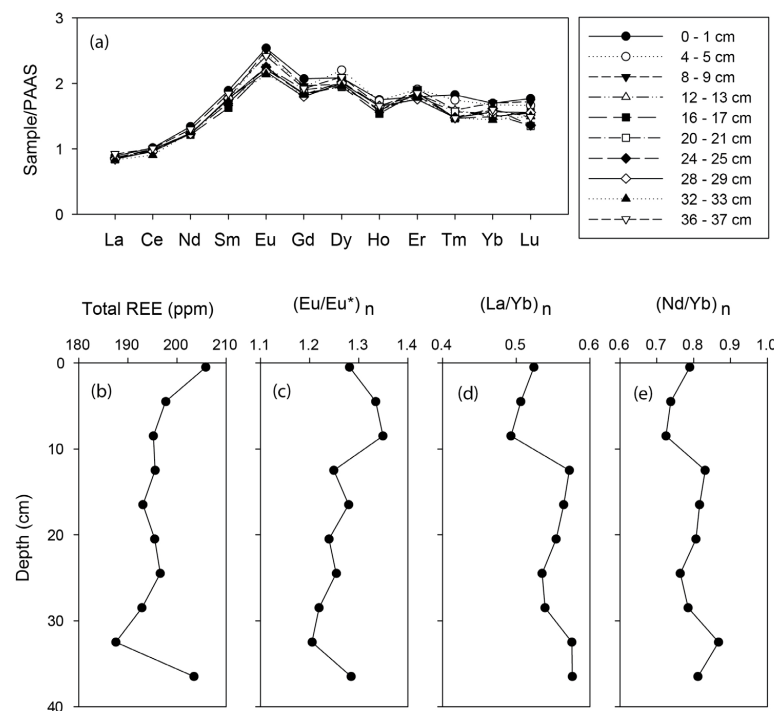


Figure 6. (a) Shale-normalized REE pattern and down-core variations of (b) total REE, (c) $(\text{Eu}/\text{Eu}^*)_n$, (d) $(\text{La}/\text{Yb})_n$, and (e) $(\text{Nd}/\text{Yb})_n$ for bulk sediments of the core BC-10.

4.3. Fe-Speciation in Sediments

The Fe concentrations determined by the sequential chemical extraction in the selected sediment samples are shown in Figure 7. Fe_{Total} represents the sum of all fractions, i.e., $Fe_{Total} = Fe_{Acetate} + Fe_{HA-HCl} + Fe_{Dithionite} + Fe_{Oxalate} + Fe_{HCl} + Fe_{Res}$. The relative magnitude of the Fe phases separated in this core follows the order: $Fe_{HA-HCl} > Fe_{Dithionite} > Fe_{HCl} > Fe_{Oxalate} > Fe_{Res} > Fe_{Acetate}$ (Figure 7.). Fe_{Total} content of the core ranges between 7.1 and 7.5 wt.%, and the vertical profile of Fe_{Total} does not show much variation with depth (Figure 5). Among the Fe phases, Fe_{HA-HCl} is the largest pool and accounts for ~30.7% of the Fe_{Total} . The concentration of Fe_{HA-HCl} extracts ranges from 1.8 to 2.89 wt.% (Table S3), and the down-core profile shows a slight decrease below the surface (10 cm). $Fe_{Dithionite}$ contents of the studied sediments are in the range of 1.17–1.57 wt.% (Table S3), and their relative percentage varies between 16.5 and 22.2% of the Fe_{Total} . The highly reactive oxides ($Fe_{HA-HCl} + Fe_{Dithionite}$) account for more than 50% of Fe_{Total} . Compared with the other oxide phases, $Fe_{Oxalate}$ content in the BC-10 is low (0.57 and 0.98 wt.%) and accounts for 11.7% of the Fe_{Total} . Fe associated with the poorly reactive sheet silicates (Fe_{HCl}) is the third-largest pool of Fe (1.18 and 1.59 wt.%), accounts for 20% of the Fe_{Total} , and the vertical profile shows a slight increase below the surface (Figure 7). The concentration of Fe_{Res} accounts for only 11.55% of the total and their concentrations vary between 0.73 and 0.90 wt.%.

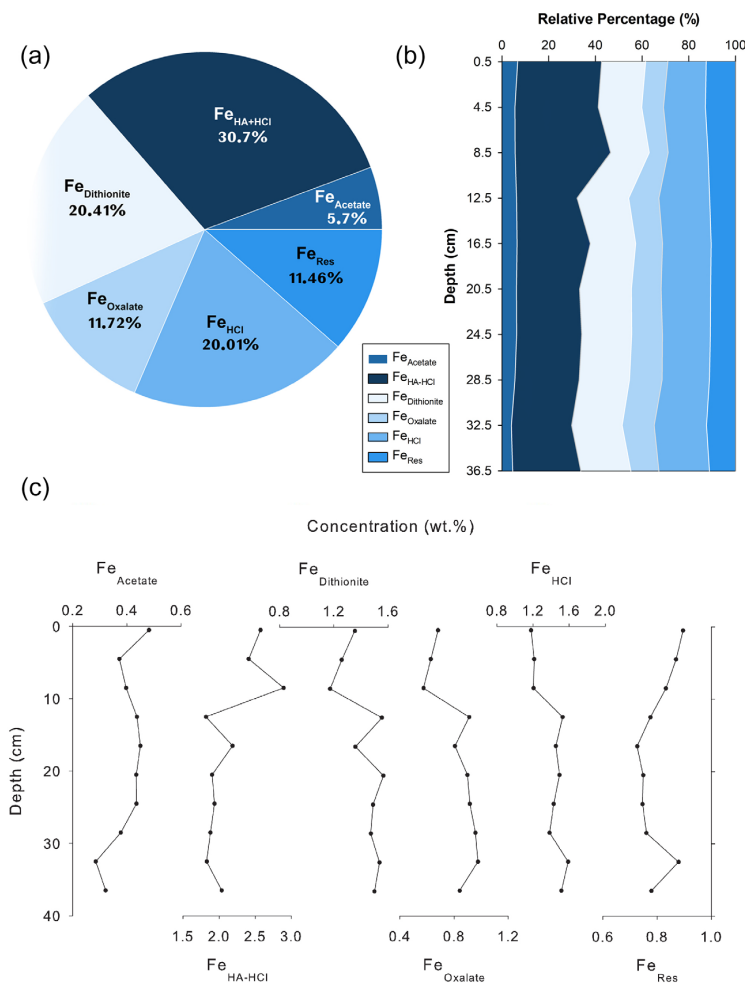


Figure 7. (a) Phase partitioning of different sedimentary iron species in the sediment core based on average data. (b) Relative percentages of solid Fe phases with sediment depth. (c) Down-core variation of different Fe phases (units in wt.%).

4.4. Statistical Analysis of Element Composition Characteristics

The elemental compositions of sediments at various depths exhibit a consistent pattern of variation, suggesting that the source characteristics of the samples are relatively consistent. The statistical characteristics of the data mainly reflect the source characteristics. A hierarchical clustering analysis was performed and six groups were identified (Figure 8). The correlation coefficient for Group I with respect to Ni, Mg, and Cr is greater than 0.8, indicating a high degree of similarity in source characteristics and likely indicating an ultramafic source. In Group II, a strong correlation is observed between Fe and Mn ($r = 0.7$), Fe and V ($r = 0.8$), as well as Fe and Al and Ti ($r = 0.9$). This suggests mixed source characteristics and the possibility of both terrigenous and hydrothermal inputs.

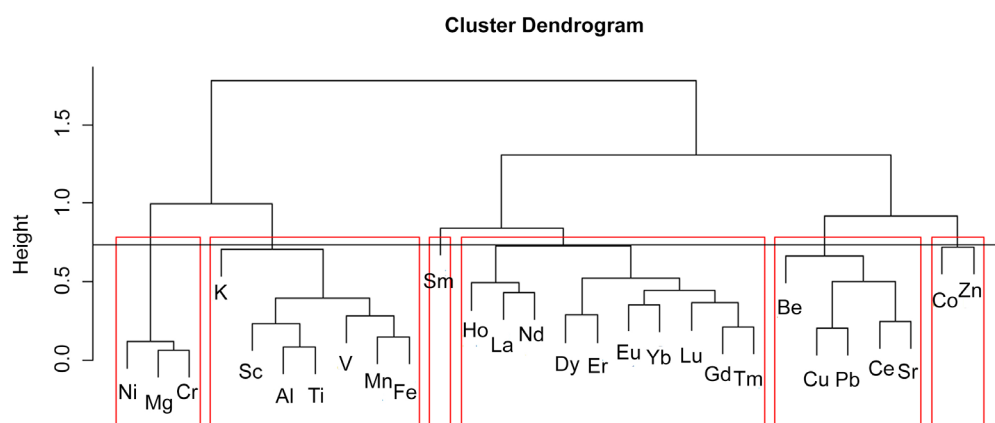


Figure 8. Cluster analysis of major and trace elements in the sediment core BC-10. Red lines indicate different groups obtained by hierarchical clustering.

5. Discussions

5.1. Characterization of Source Components

5.1.1. Hydrothermal Source

Major components of mid-oceanic ridge sediments are a mixture of biogenic carbonates, detrital sediments, and volcanic/hydrothermal-derived materials. High Fe concentration and magnetic susceptibility values in the present studied core are a direct indication of metalliferous components since the enrichment of Fe and Mn occurs mainly through hydrothermal input. There are known hydrothermal fields, such as Mt. Jourdanne, Tiancheng, and Tianzuo, in the vicinity of the core location [22–24]. Aluminium and titanium contents of the sediments can be used as terrigenous/detrital indicators since these elements are refractory and least susceptible to alteration [40,41]. Sediments altered by hydrothermal activity show distinct geochemical characteristics compared with the background sediments [42]. The metalliferous sediment index ($MSI = Al / (Fe + Mn + Al) \times 100$) can be used to discriminate metalliferous sediments from pelagic sediments [43]. A MSI value of >50 represents pelagic sediments with terrigenous/detrital components, whereas a lower value indicates the presence of metalliferous/hydrothermal components in the samples [15,44]. The calculated MSI value of the samples varies between 42.8 and 45%, suggesting slight enrichment of metalliferous components in the sediment core. These values are comparable with the hydrothermally altered sediments at a seamount flank of CIB (MSI—40–44) [39] and are higher than the Rainbow hydrothermal field (MSI—20–25) [44].

The ratios of Co/Zn can be used to discriminate the hydrothermal and hydrogenous origin of sediments, considering Co as an element of hydrogenous origin while Zn is from a hydrothermal source [39]. The trace element data of BC-10 shows very low Co/Zn ratios close to the hydrothermal origin (~0.5). The scatter plot of (Co + Ni + Cu) versus Co/Zn of bulk sediments is very closely spaced and suggests hydrothermal components throughout the sediment core (Figure 9). The Zn/Fe ratios are comparable (1.9–2.5) to the metalliferous sediments of the Central Indian basin [39] and hydrothermal Fe-oxides

of other regions. These samples fall in the hydrothermal field in the ternary diagram of Fe, Mn vs. $(\text{Co} + \text{Ni} + \text{Cu}) \times 10$ (Figure 9). All these collectively indicate the presence of hydrothermal signatures in the sediment core. However, compared with the near-field metalliferous sediments [20,44], the concentrations of Cu and Zn in the studied core are low. The high input of Cu and Zn occurs proximal to the hydrothermal vent field and decreases with distance from the field [45]. The consistent enrichment in the average concentrations of Fe, Mn, V, and Cu in BC-10 sediments compared with the background sediments from SWIR reported by Liao et al. [18] also suggests the presence of metalliferous components in the sediment core.

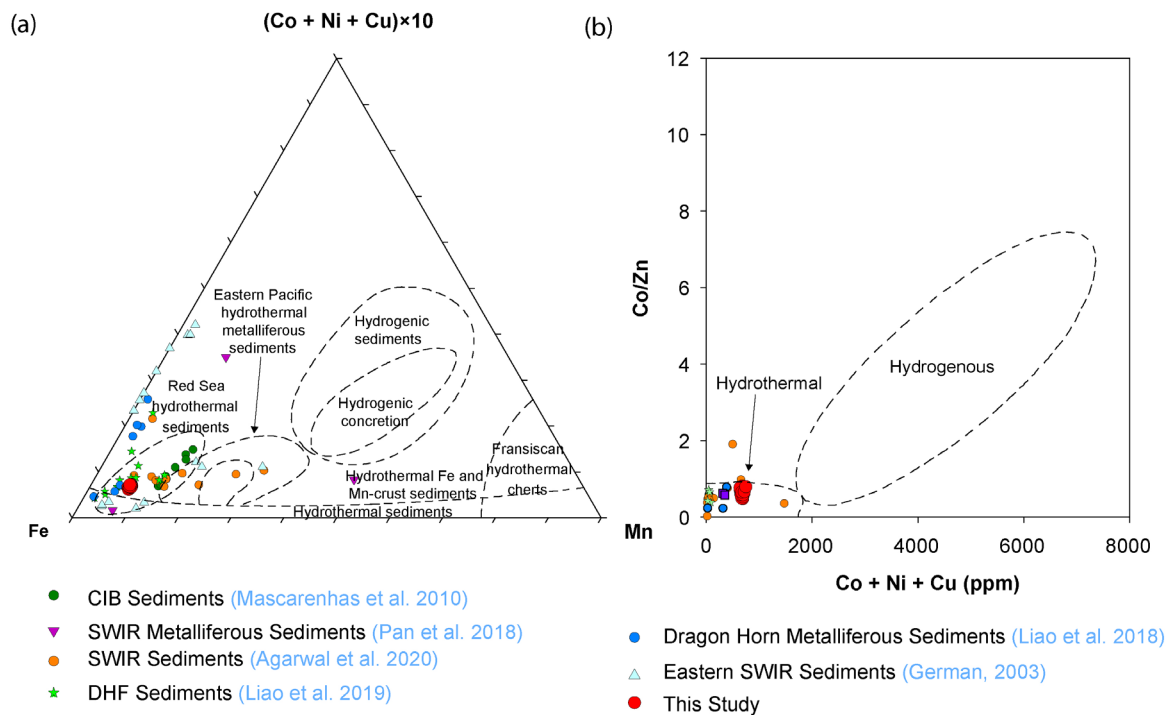


Figure 9. (a) Fe-Mn-(Co + Ni + Cu) $\times 10$ ternary (Modified from [46]). (b) Scatter plot of Co/Zn ratio versus Cu + Ni + Co content of the sediment core (Modified from [39]). Data points are taken from different sources, Metalliferous Sediments from Central Indian Ocean (CIB) [39], Metalliferous Sediments, SWIR [13,20], Duanqiao-1 hydrothermal field Sediments [19], Dragon Horn Metalliferous Sediments [18], Eastern SWIR Sediments [15].

The concentrations of total REE range between 184 and 206 $\mu\text{g/g}$ (Table S2). The total REE content of the sediments is significantly lower than the metalliferous sediments from the Central Indian Basin [39] and higher than the metalliferous sediments from the Mid-Atlantic Ridge [44]. REE (carbonate-free basis) contents of the studied core are comparable with the metalliferous sediments from the SWIR [18].

Post-Archean Australian shale-normalized REE pattern of the bulk sediments shows lighter REE depletion (Figure 6). $(\text{La}/\text{Yb})_n$ ratios vary between 0.49 and 0.60, indicating the HREE enrichment in sediments (Figure 6). HREE enrichment in sediments indicates hydrothermal activity [39]. Positive Eu anomaly in sediments (Figure 6) also suggests the presence of hydrothermal components in sediments. The general trend of HREE enrichment and positive Eu anomaly of BC-10 are similar to metalliferous sediments from the East Pacific Rise [37].

Rare-earth elements in sediments can be used to discriminate plume-derived sediments from oxidized materials and slumped sulphides [9,47,48], and the REE pattern of the sediment reflects the extent of hydrothermal alterations [49]. Hydrothermal fluid exhibits a large positive Eu anomaly and LREE enrichments, whereas seawater exhibits negative Ce anomaly

and HREE enrichment [48]. Fe and Mn oxyhydroxides in sediments strongly control REE geochemistry. During the rising and dispersal of hydrothermal fluid, Fe-Mn oxides and oxyhydroxides scavenge REE from seawater, leading to the net removal of REE from seawater since the hydrothermally sourced Fe-Mn oxides have a high specific area and surface charge [48,50]. However, the REE content scavenged by Fe-Mn oxyhydroxides depends on the interaction time and distance from the hydrothermal vent site [51]. A strong positive correlation of the Eu anomaly between amorphous ferrihydrite and Mn oxides fraction suggests that Fe-Mn oxyhydroxides strongly control the REE geochemistry in the present studied samples. Down-core variations of the La/Yb ratio of the sediments also show a strong positive correlation with the Fe_{HA-HCl} phase. This indicates that the fractionation of REE in the presently studied sediments is strongly linked with the ferrihydrite in samples.

5.1.2. Mafic and Ultramafic Sources

The cluster analysis of the studied sediment suggests mixed source characteristics. Thus, for understanding the basaltic contribution in the studied samples, we used the ternary diagram of Al + K-Fe + Mn-Mg (Figure 10). The sediments composed of basaltic debris distribute towards the Al + K vertex, whereas hydrothermal sediments distribute close to Fe + Mn endmember since they are enriched with Fe and Mn and depleted in Al and K [52]. The Al + K-Fe + Mn-Mg ternary diagram (Figure 10) shows that BC-10 samples distribute close to the hydrothermally altered basaltic debris from the SWIR [53], suggesting the presence of hydrothermally altered basaltic debris in the samples.

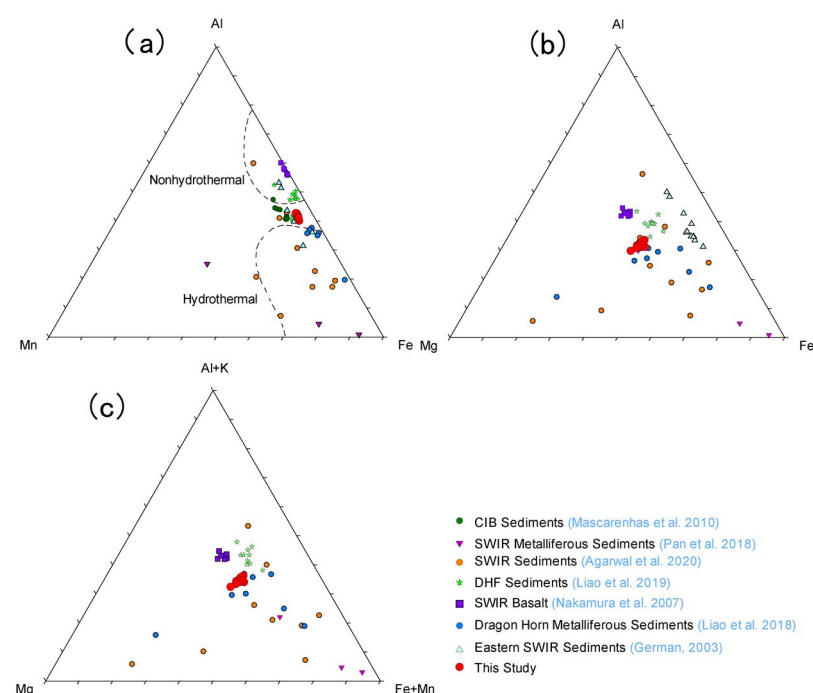


Figure 10. (a) Fe-Mn-Al ternary diagram (modified from [54]). (b) Fe-Mg-Al ternary diagram. (c) Al + K-Mg-Fe + Mn ternary diagram for BC-10 core and comparison with other studies. Data points are taken from different sources, Metalliferous Sediments from Central Indian Ocean (CIB) [39], Metalliferous Sediments, SWIR [13,20], Duanqiao-1 hydrothermal field Sediments [19], Dragon Horn Metalliferous Sediments [18], SWIR Basalt [53], Eastern SWIR Sediments [15].

Magnesium concentrations of the presently studied sediments are relatively high compared with the other metalliferous sediments from the CIB [39]. A high Mg content directly indicates mafic/ultramafic components in sediments. Agarwal et al. [13] also reported high Mg content at one of the stations, E-7-29 (16.80 wt.%), which is located near the Tianzuo hydrothermal field (27°57' S, 63°32' E) is an inactive sulphide hydrothermal field hosted by ultramafic rocks associated with

detachment faults [23,55,56]. Thus, the Tianzuo hydrothermal field could be the source for the high Mg present in the present studied core. The Tianzuo field is situated on a dome-shaped structure, and hydrothermal activities are controlled by detachment fault [55]. As the present studied sediment core is located in the valley, the debris flow from the Tianzuo field could be a major source of sediments in this area. The nearby Tiancheng hydrothermal field is hosted by basaltic rocks, which are low in Mg [23], thereby suggesting an increased contribution from Tianzuo to this area.

In the present study, the sediments show a high concentration of Pb (25.1–34.8 $\mu\text{g/g}$) and are slightly higher when compared with the metalliferous sediments from SWIR (Pb- 13.6 $\mu\text{g/g}$, [14]). The enrichment of Pb in hydrothermal deposits mainly occurs due to fluid alteration, whereas in deep-sea sediments, combined magmatism and rock-fluid interaction can lead to Pb enrichment, especially in peridotites [57]. Cluster analysis results show a positive correlation between Pb and Cu, suggesting their association through a common source. Previous studies also demonstrated that peridotite-hosted hydrothermal fields such as Logatchev and Rainbow show higher Pb concentrations compared with basalt-hosted hydrothermal fields such as TAG and Snake Pit [58]. Concentrations of nickel (avg. 352 $\mu\text{g/g}$) and chromium (avg. 292 $\mu\text{g/g}$) are high in the presently studied sediments; this may be because of the contribution from peridotites in which Ni is enriched when compared with basaltic rocks, whereas Cr is usually high in pyroxenes compared with olivine and serpentinization of pyroxene can enrich both aluminium and chromium [59]. The overall enrichment of Pb, Ni, and Cr in the samples indicates mafic as well as an ultramafic source together with the hydrothermal components. Further, the present location of the sediment core is close to the ultramafic-hosted Tianzuo hydrothermal field and confirms the source characteristics of these sediments. In the ternary diagrams of Fe-Mn-Al and Fe-Mg-Al (Figure 10), BC-10 samples fall close to the metalliferous sediments from the Fuji Dome studied by Agarwal et al. [13], Dragon Horn area [18], and far-field metalliferous sediments from the SWIR [20]. Dragon Horn hydrothermal sediments are a mixture of pelagic sediments, local mafic, ultramafic debris, and hydrothermal components [18]. This suggests that mafic and ultramafic debris are also present in our sediment core along with the hydrothermal components.

5.2. Geochemical Characteristics of Fe in the Sediment Core

The sequential chemical extraction results indicate that among the Fe phases, $\text{Fe}_{\text{HA-HCl}}$ (ferrihydrite and lepidocrocite) forms the largest pool and accounts for ~30% of the Fe_{Total} (Figure 7). As explained in the previous section, it is evident that the sediment core in the study area has a contribution from the nearby hydrothermal field. The oxidation and precipitation of Fe during the plume dispersal resulted in a high content of $\text{Fe}_{\text{HA-HCl}}$. This result is consistent with previous studies, which found that most of the Fe in hydrothermal plumes consists of Fe oxyhydroxides [60,61]. Among the Fe oxides, ferrihydrite is a commonly found mineral in the sediments proximal to the hydrothermal vents along mid-oceanic ridges [62].

However, the hydrogenous precipitation also leads to the enrichment of poorly crystalline Fe-oxides in the study area. The bulk geochemistry of the present study (Figures 6 and 9) indicates hydrothermal formation rather than hydrogenous precipitation. REE geochemistry can be used to distinguish hydrothermal precipitation from hydrogenous precipitation [63]. We plotted the Ce anomaly and Nd_n/Yb_n ratio to distinguish the hydrogenous and hydrothermal precipitation (Figure 11). Generally, hydrogenous precipitation shows positive Ce anomaly, and REE fractionation (Nd_n/Yb_n) is controlled by either hydrothermal plume particulates or low-temperature fluid input [63]. Our result suggests the hydrothermal plume particulates (as shown by REE fractionation) are major contributors for REE in these samples.

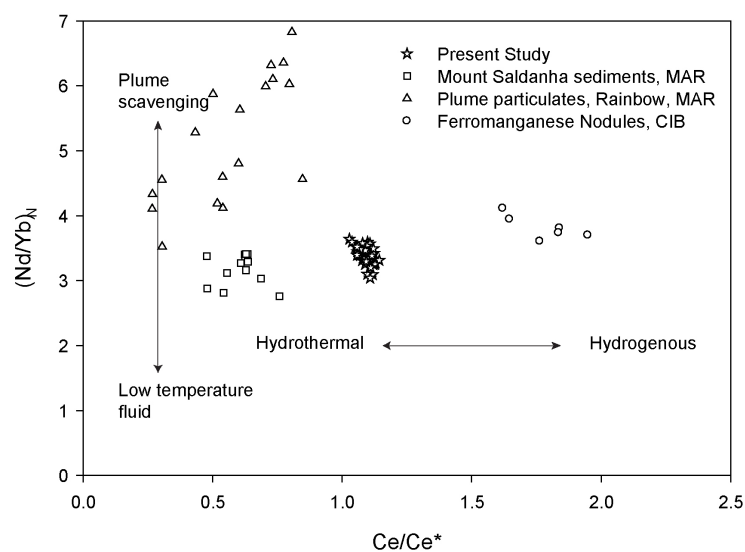


Figure 11. Plot of Nd/Yb_N against Ce/Ce^* for the BC-10 core comparison with other studies. Data points are taken from different sources, Mount Saldanha sediments from Mid Atlantic Ridge [64], Plume particulates from Rainbow Hydrothermal Field [65], and ferromanganese nodules from Central Indian Basin [66].

The $Fe_{Dithionite}$ phase, consisting of minerals such as hematite and goethite, constitutes the second largest pool of Fe and accounts for $\sim 20.4\%$ of the Fe_{Total} (Figure 7). Most of the ferrihydrite derived from the hydrothermal sources are unstable and transform into more structurally ordered phases such as goethite and hematite [6]. However, several factors, such as pH, the concentration of certain elements, bacteria, etc., can control the transformation of ferrihydrite into more crystalline phases [6,62,67–69]. At neutral pH conditions, the transformation of ferrihydrite to hematite is favoured over goethite [67]. However, certain elements such as Ti alter this scenario and favor goethite formation [6,68]. Down-core variation of Fe_{HA-HCl} shows slight enrichment at the surface and decrease down the core (Figure 7), whereas the $Fe_{Dithionite}$ is depleted at the surface with an enrichment below the surface, indicating the transformation of ferrihydrite to a more crystalline phase (goethite/hematite). The vertical profile of Fe_{HA-HCl} and $Fe_{Dithionite}$ are mirror images of each other, and these could reflect the formation of $Fe_{Dithionite}$ at the expense of Fe_{HA-HCl} .

Even though the transformation of ferrihydrite is taking place, the Fe_{HA-HCl} content is still high throughout the core (Figure 7), implicating the slow rate of ferrihydrite transformation. A relatively slow rate of ferrihydrite transformation seen in this study is consistent with a previous study from the south Eastern Pacific Rise, which estimated a half-life of 2.32 ± 0.07 My for ferrihydrite transformation [6]. Freshly precipitated ferrihydrite rapidly transforms to more stable mineral phases, while co-precipitation of transition metals and oxyanions within the ferrihydrite crystals and the presence of bacteria retard this transformation [6,62,69,70].

$Fe_{Oxalate}$ content is relatively low compared with other oxides and accounts for an average of 11.7% of the Fe_{Total} . The formation of magnetite generally occurs under redox conditions, but a non-redox transformation of primary precipitate (hematite/goethite) to magnetite can occur in a hydrothermal environment [71]. Magnetite formation in a hydrothermal environment occurs either through the crystallization of magnetite at high temperatures from silicate and sulphide melts or due to the precipitation at low temperatures from hydrothermal fluids [72–75]. Thus, $Fe_{Oxalate}$ contents are relatively low in far-field hydrothermal sediments compared with near-field hydrothermal sediments. The down-core profile of $Fe_{Oxalate}$ shows slight enrichment below the surface, which could be due to the depositional changes of hydrothermal components since magnetite is less reactive than the other Fe-oxide/hydroxides.

Iron associated with the poorly reactive sheet silicates constitutes (Fe_{HCl}) the third-largest pool of Fe phases, accounting for ~20% of the Fe_{Total} (Figure 7). The down-core variation of Fe_{HCl} is similar to the $Fe_{Dithionite}$ variations (Figure 7), with a positive linear correlation ($R^2=0.84$), suggesting a common source. Fe-oxyhydroxides intermixed with clay minerals are major components of hydrothermal sediments and are formed by the interaction of the hydrothermal fluid with basalts, metalliferous sediments, and biogenic sediments [76,77]. The clay minerals formed in such an environment are generally enriched by Fe and Mg [77]. High concentrations of Mg measured in the Fe_{HCl} phase (32% of the total Mg) with Fe also support this finding. Such Fe-Mg-Silicates are also reported in the hydrothermal plumes from the Central Indian Ridge [78] and Carlsberg Indian Ridge [79].

The Fe precipitation with silica and Mg is commonly observed in hydrothermal systems associated with ultramafic rocks. Recent studies by Qiu et al. [80] in near-field sediments collected from ultramafic-hosted Tianxiu field, Carlsberg Ridge, also show high Mg concentrations. Therefore, the high Mg concentration associated with the Fe_{HCl} phase may be from the ultramafic-hosted Tianzuo hydrothermal field. Apart from this, the diagenetic formation of Fe-silicates at the expense of ferrihydrite dissolution is also common in hydrothermal sediments [6]. Thus, the down-core increase of Fe_{HCl} and a corresponding decrease in Fe_{HA-HCl} over the top 10 cm is due to the transformation of ferrihydrite to Fe_{HCl} (Figure 7).

Fe_{Res} representing iron associated with un-reactive sheet silicates and pyrite are low in these sediments (11.4%) (Figure 7). When a hydrothermal plume emerges from the vent, ~50% of Fe precipitates rapidly as Fe sulphide [81–84]. Thus, most of the Fe-sulphides are found proximal to the hydrothermal field (approximately within 1.5 km of the hydrothermal vent field), and their concentration decreases with increasing distance from the vent [85,86]. The possibility of pyrite formation during the plume dispersal is ruled out in our study area since the BC-10 location is 12.5 km (Tianzuo) and 32 km (Tiancheng and Mt. Jourdanne) away from the reported hydrothermal fields. However, XRD analysis of the BC-10 samples clearly shows the presence of pyrite in the sediments. These could be due to the sulphide debris transported from the nearby vent fields through sediment flows. Aluminium and magnesium measured in the residual fraction indicate that ~56% of Al and 22% of the Mg are associated detrital phase (Table S4). The bulk geochemistry of the studied core shows basaltic/ultramafic components in the sediments (Figures 9 and 10). Thus, our results indicate that most of the Fe in Fe_{Res} is associated with the detrital phase rather than pyrite. However, compared with other phases, the concentration of Fe associated with the residual phase is low and plays a minor role in the sedimentary cycling of Fe in this area.

6. Conclusions

The mineralogical and geochemical investigations of a short sediment core collected near the Tianzuo hydrothermal field from the SWIR indicate that the sediments are a mixture of basaltic, ultramafic, and hydrothermal components. The presence of volcanogenic glass shards and phillipsite throughout the sediment core confirms the local volcanic activities and their transformation to low-temperature alteration products in the proximity to this area. The major and trace and rare-earth element data of the core reveal the influence of hydrothermal activities on the sediments. The shale-normalized REE pattern shows positive Eu anomaly and HREE enrichment in the sediment core, reflecting the presence of metalliferous components in the sediments. Results of the sequential chemical extraction of Fe indicate that the dominant mineral phase of Fe is Fe_{HA-HCl} (indicative of ferrihydrite and lepidocrocite), followed by $Fe_{Dithionite}$, Fe_{HCl} , $Fe_{Oxalate}$, Fe_{Res} , and $Fe_{Acetate}$. Vertical profiles of different fractions indicate the formation of crystalline Fe-oxides and Fe-silicates at the expense of ferrihydrite dissolution. The concentration of Fe associated with Fe_{Res} may suggest the role of Fe-sulphides eroded from the nearby vent field.

Supplementary Materials: The following supporting information can be downloaded at: <https://www.mdpi.com/article/10.3390/min13020209/s1>. Table S1: Major and trace element concentrations and elemental ratios in bulk sediments of BC-10 core; Table S2: Rare earth element concentrations, Eu/Eu*, Ce/Ce* and elemental ratios in bulk sediments of BC-10 core; Table S3: Down core variation of different Fe phases in BC-10 core; Table S4: Average relative percentages of Mn, Al, and Mg measured in different Fe phases.

Author Contributions: Conceptualization, P.L., L.S.P. and P.J.K.; methodology, P.L.; software, P.R. and M.S.; validation, P.L., L.S.P. and P.J.K.; formal analysis, P.L.; investigation, P.L.; resources, P.J.K. and P.R.; data curation, P.L., L.S.P., M.S. and P.R.; writing—original draft preparation, P.L.; writing—review and editing, P.L., L.S.P., P.R., M.S. and P.J.K.; visualization, P.L. and M.S.; supervision, P.J.K. and P.R.; project administration, P.J.K. and P.R.; funding acquisition, P.J.K. All authors have read and agreed to the published version of the manuscript.

Funding: This work was undertaken as part of the Hydrothermal Sulphides Program with Grant No. MOES/EFC/28/2018-II funded by the Ministry of Earth Sciences, Government of India.

Data Availability Statement: Not applicable.

Acknowledgments: The authors thank the Director National Centre for Polar and Ocean Research, Goa, for permitting this work to be published. We are thankful to B Nagender Nath for his valuable suggestions, which helped to improve the quality of the manuscript. The authors would also like to thank T. Meloth, W. Rahaman, Lathika, Vineeta, and Tarique for providing access to the ICP-MS facility. We are thankful to Sahina Gazi and Rahul Mohan for SEM-EDS analyses and M. Tiwari, Vikas, and Viola for their help with ICP-OES analyses. We are thankful to Sourav for his help in cluster analysis. We are thankful to Girish A. Prabhu, CSIR-NIO, for carrying out the XRD analysis. This is NCPOR contribution No: J-63/2022-23.

Conflicts of Interest: The authors declare no conflict of interest. The funders had no role in the design of the study; in the collection, analyses, or interpretation of data; in the writing of the manuscript; or in the decision to publish the results.

References

1. Rona, P.A.; Bemis, K.G.; Jones, C.D.; Jackson, D.R.; Mitsuzawa, K.; Silver, D. Entrainment and Bending in a Major Hydrothermal Plume, Main Endeavour Field, Juan de Fuca Ridge. *Geophys. Res. Lett.* **2006**, *33*, 6–11. [[CrossRef](#)]
2. Rouxel, O.; Toner, B.M.; Manganini, S.J.; German, C.R. Geochemistry and Iron Isotope Systematics of Hydrothermal Plume Fall-out at East Pacific Rise 9°50' N. *Chem. Geol.* **2016**, *441*, 212–234. [[CrossRef](#)]
3. Baker, E.T.; Massoth, G.J.; Feely, R.A.; Embley, R.W.; Richard, E.; Thomson Brenda, J. Burd Hydrothermal Event Plumes from the CoAxial Seafloor Eruption Site, Juan de Fuca Ridge. *Geophys. Res. Lett.* **1995**, *22*, 147–150. [[CrossRef](#)]
4. Bennett, S.A.; Achterberg, E.P.; Connelly, D.P.; Statham, P.J.; Fones, G.R.; German, C.R. The Distribution and Stabilisation of Dissolved Fe in Deep-Sea Hydrothermal Plumes. *Earth Planet. Sci. Lett.* **2008**, *270*, 157–167. [[CrossRef](#)]
5. Tagliabue, A.; Bopp, L.; Dutay, J.C.; Bowie, A.R.; Chever, F.; Jean-Baptiste, P.; Bucciarelli, E.; Lannuzel, D.; Remenyi, T.; Sarthou, G.; et al. Hydrothermal Contribution to the Oceanic Dissolved Iron Inventory. *Nat. Geosci.* **2010**, *3*, 252–256. [[CrossRef](#)]
6. Poulton, S.W.; Canfield, D.E. Co-Diagenesis of Iron and Phosphorus in Hydrothermal Sediments from the Southern East Pacific Rise: Implications for the Evaluation of Paleoseawater Phosphate Concentrations. *Geochim. Cosmochim. Acta* **2006**, *70*, 5883–5898. [[CrossRef](#)]
7. Feely, R.A.; Massoth, G.J.; Baker, E.T.; Lebon, G.T.; Geiselman, T.L. Tracking the Dispersal of Hydrothermal Plumes from the Juan de Fuca Ridge Using Suspended Matter Compositions. *J. Geophys. Res. Solid Earth* **1992**, *97*, 3457–3468. [[CrossRef](#)]
8. Feely, R.A.; Baker, E.T.; Marumo, K.; Urabe, T.; Ishibashi, J.; Gendron, J.; Lebon, G.T.; Okamura, K. Hydrothermal Plume Particles and Dissolved Phosphate over the Superfast-Spreading Southern East Pacific Rise. *Geochim. Cosmochim. Acta* **1996**, *60*, 2297–2323. [[CrossRef](#)]
9. German, C.R.; Hergt, J.; Palmer, M.R.; Edmond, J.M. Geochemistry of a Hydrothermal Sediment Core from the OBS Vent-Field, 21° N East Pacific Rise. *Chem. Geol.* **1999**, *155*, 65–75. [[CrossRef](#)]
10. Gartman, A.; Findlay, A.J. Impacts of Hydrothermal Plume Processes on Oceanic Metal Cycles and Transport. *Nat. Geosci.* **2020**, *13*, 396–402. [[CrossRef](#)]
11. German, C.R.; Campbell, A.C.; Edmond, J.M. Hydrothermal Scavenging at the Mid-Atlantic Ridge: Modification of Trace Element Dissolved Fluxes. *Earth Planet. Sci. Lett.* **1991**, *107*, 101–114. [[CrossRef](#)]
12. Sander, S.G.; Koschinsky, A. The Export of Iron and Other Trace Metals from Hydrothermal Vents and the Impact on Their Marine Biogeochemical Cycle. In *Trace Metal Biogeochemistry and Ecology of Deep-Sea Hydrothermal Vent Systems*; Springer: Berlin/Heidelberg, Germany, 2016; Volume 50, pp. 9–24. ISBN 1433-6839.

13. Agarwal, D.K.; Roy, P.; Prakash, L.S.; Kurian, P.J. Hydrothermal Signatures in Sediments from Eastern Southwest Indian Ridge 63° E to 68° E. *Mar. Chem.* **2020**, *218*, 103732. [[CrossRef](#)]
14. Chen, X.; Sun, X.; Wu, Z.; Wang, Y.; Lin, X.; Chen, H. Mineralogy and Geochemistry of Deep-Sea Sediments from the Ultraslow-Spreading Southwest Indian Ridge: Implications for Hydrothermal Input and Igneous Host Rock. *Minerals* **2021**, *11*, 1–38. [[CrossRef](#)]
15. German, C.R. Hydrothermal Activity on the Eastern SWIR (50°–70°E): Evidence from Core-Top Geochemistry, 1887 and 1998. *Geochem. Geophys. Geosyst.* **2003**, *4*, 1–13. [[CrossRef](#)]
16. Kalangutkar, N.G.; Kurian, P.J.; Iyer, S.D. Characterization of Ferromanganese Crusts from the Central and South West Indian Ridges: Evidence for Hydrothermal Activity. *Mar. Geores. Geotechnol.* **2021**, *40*, 281–296. [[CrossRef](#)]
17. Li, Z.; Chu, F.; Jin, L.; Li, X.; Dong, Y.; Chen, L.; Zhu, J. Major and Trace Element Composition of Surface Sediments from the Southwest Indian Ridge: Evidence for the Incorporation of a Hydrothermal Component. *Acta Oceanol. Sin.* **2016**, *35*, 101–108. [[CrossRef](#)]
18. Liao, S.; Tao, C.; Li, H.; Zhang, G.; Liang, J.; Yang, W.; Wang, Y. Surface Sediment Geochemistry and Hydrothermal Activity Indicators in the Dragon Horn Area on the Southwest Indian Ridge. *Mar. Geol.* **2018**, *398*, 22–34. [[CrossRef](#)]
19. Liao, S.; Tao, C.; Dias, Á.A.; Su, X.; Yang, Z.; Ni, J.; Liang, J.; Yang, W.; Liu, J.; Li, W.; et al. Surface Sediment Composition and Distribution of Hydrothermal Derived Elements at the Duanqiao-1 Hydrothermal Field, Southwest Indian Ridge. *Mar. Geol.* **2019**, *416*, 105975. [[CrossRef](#)]
20. Pan, A.; Yang, Q.; Zhou, H.; Ji, F.; Wang, H.; Pancost, R.D. Geochemical Impacts of Hydrothermal Activity on Surface Deposits at the Southwest Indian Ridge. *Deep. Res. Part I Oceanogr. Res. Pap.* **2018**, *139*, 1–13. [[CrossRef](#)]
21. Surya Prakash, L.; Ray, D.; Nagender Nath, B.; Satyanarayanan, M.; Kamesh, K.R.; Kurian, J.P.; Dileep Kumar, M.; Srinivas Rao, A. Anomalous Phase Association of REE in Ferromanganese Crusts from Indian Mid-Oceanic Ridges: Evidence for Large Scale Dispersion of Hydrothermal Iron. *Chem. Geol.* **2020**, *549*, 119679. [[CrossRef](#)]
22. Beaulieu, S.; Szafranski, K. InterRidge Global Database of Active Submarine Hydrothermal Vent Fields. 2010. Available online: <https://vents-data.interridge.org/> (accessed on 25 April 2021).
23. Chen, J.; Tao, C.; Liang, J.; Liao, S.; Dong, C.; Li, H.; Li, W.; Wang, Y.; Yue, X.; He, Y. Newly Discovered Hydrothermal Fields along the Ultraslow-Spreading Southwest Indian Ridge around 63° E. *Acta Geol. Sin.* **2018**, *37*, 61–67. [[CrossRef](#)]
24. Tao, C.; Wu, G.; Ni, J.; Zhao, H.; Su, X.; Zhou, N.; Li, J.; Chen, Y.J.; Cui, R.; Deng, X.; et al. New Hydrothermal Fields Found along the SWIR during the Legs 5-7 of the Chinese DY115-20 Expedition. *AGU Fall Meet. Abstr.* **2009**, *2009*, S21A–S1150A.
25. Marks, K.M.; Tikku, A.A. Cretaceous Reconstructions of East Antarctica, Africa and Madagascar. *Earth Planet. Sci. Lett.* **2001**, *186*, 479–495. [[CrossRef](#)]
26. Dick, H.J.B.; Lin, J.; Schouten, H. An Ultraslow-Spreading Class of Ocean Ridge. *Nature* **2003**, *426*, 405–412. [[CrossRef](#)]
27. Cannat, M.; Sauter, D.; Ruellan, E.; Okino, K.; Escartin, J.; Combier, V. Modes of Seafloor Generation at a Melt-Poor Ultraslow-Spreading Ridge. *Geology* **2006**, *34*, 605. [[CrossRef](#)]
28. Zhou, H.; Dick, H.J.B. Thin Crust as Evidence for Depleted Mantle Supporting the Marion Rise. *Nature* **2013**, *494*, 199–200. [[CrossRef](#)]
29. Han, Z.; Zhang, H.; Fan, D.; Ding, M.; Liu, M.; Xu, C. The Characteristic of Geochemistry and Genesis for Mafic and Ultramafic Rocks from the 50° E of Southwest Indian Ridge. *Period. Ocean Univ. China* **2012**, *42*, 69–76.
30. Chen, Y.Y.; Yu, B.S.; Su, X.; Yu, M. Mineralogical and Geochemical Characteristics of the Calcareous Sediments in Southwest Indian Ridge. *Geol. Sci. Technol. Inf.* **2013**, *32*, 107–113.
31. Münch, U.; Halbach, P.; Fujimoto, H. Sea-Floor Hydrothermal Mineralization from the Mt. Jourdanne, Southwest Indian Ridge. *AMSTEC J. Deep Sea Res* **2000**, *16*, 125–132.
32. Poulton, S.W.; Canfield, D.E. Development of a Sequential Extraction Procedure for Iron: Implications for Iron Partitioning in Continentally Derived Particulates. *Chem. Geol.* **2005**, *214*, 209–221. [[CrossRef](#)]
33. Slotznick, S.P.; Swanson-Hysell, N.L.; Sperling, E.A. Oxygenated Mesoproterozoic Lake Revealed through Magnetic Mineralogy. *Proc. Natl. Acad. Sci. USA* **2018**, *115*, 12938–12943. [[CrossRef](#)]
34. Bauer, K.W.; Byrne, J.M.; Kenward, P.; Simister, R.L.; Michiels, C.C.; Friese, A.; Vuillemin, A.; Henny, C.; Nomosatryo, S.; Kallmeyer, J.; et al. Magnetite Biomineralization in Ferruginous Waters and Early Earth Evolution. *Earth Planet. Sci. Lett.* **2020**, *549*, 116495. [[CrossRef](#)]
35. Sun, Z.; Zhou, H.; Glasby, G.P.; Yang, Q.; Yin, X.; Li, J.; Chen, Z. Formation of Fe–Mn–Si Oxide and Nontronite Deposits in Hydrothermal Fields on the Valu Fa Ridge, Lau Basin. *J. Asian Earth Sci.* **2012**, *43*, 64–76. [[CrossRef](#)]
36. Jambor, J.; Dutrizac, J. Occurrence and Constitution of Natural and Synthetic Ferrihydrite, a Widespread Iron Oxyhydroxide. *Chem. Rev.* **1998**, *98*, 2549–2586. [[CrossRef](#)]
37. Bodei, S.; Buatier, M.; Steinmann, M.; Adatte, T.; Wheat, C.G. Characterization of Metalliferous Sediment from a Low-Temperature Hydrothermal Environment on the Eastern Flank of the East Pacific Rise. *Mar. Geol.* **2008**, *250*, 128–141. [[CrossRef](#)]
38. Kolla, V.; Bé, A.W.H.; Biscaye, P.E. Calcium Carbonate Distribution in the Surface Sediments of the Indian Ocean. *J. Geophys. Res.* **1976**, *81*, 2605–2616. [[CrossRef](#)]
39. Mascarenhas-Pereira, M.B.L.; Nath, B.N. Selective Leaching Studies of Sediments from a Seamount Flank in the Central Indian Basin: Resolving Hydrothermal, Volcanogenic and Terrigenous Sources Using Major, Trace and Rare-Earth Elements. *Mar. Chem.* **2010**, *121*, 49–66. [[CrossRef](#)]

40. Nath, B.N.; Rao, V.P.; Becker, K.P. Geochemical Evidence of Terrigenous Influence in Deep-Sea Sediments up to 8° S in the Central Indian Basin. *Mar. Geol.* **1989**, *87*, 301–313. [[CrossRef](#)]
41. Nath, B.N.; Gupta, S.M.; Mislankar, P.G.; Rao, B.R.; Parthiban, G.; Roelandts, I.; Patil, S.K. Evidence of Himalayan Erosional Event at ~0.5° Ma from a Sediment Core from the Equatorial Indian Ocean in the Vicinity of ODP Leg 116 Sites. *Deep Sea Res. Part II Top. Stud. Oceanogr.* **2005**, *52*, 2061–2077. [[CrossRef](#)]
42. Nath, B.N.; Borole, D.V.; Aldahan, A.; Patil, S.K.; Mascarenhas-Pereira, M.B.L.; Possnert, G.; Ericsson, T.; Ramaswamy, V.; Gupta, S.M. 210Pb, 230Th, and 10Be in Central Indian Basin Seamount Sediments: Signatures of Degassing and Hydrothermal Alteration of Recent Origin. *Geophys. Res. Lett.* **2008**, *35*, 2–7. [[CrossRef](#)]
43. Boström, K.; Peterson, M.N.A. The Origin of Aluminum-Poor Ferromanganous Sediments in Areas of High Heat Flow on the East Pacific Rise. *Mar. Geol.* **1969**, *7*, 427–447. [[CrossRef](#)]
44. Cave, R.R.; German, C.R.; Thomson, J.; Nesbitt, R.W. Fluxes to Sediments Underlying the Rainbow Hydrothermal Plume at 36° 14' N on the Mid-Atlantic Ridge. *Geochim. Cosmochim. Acta* **2002**, *66*, 1905–1923. [[CrossRef](#)]
45. Liao, S.; Tao, C.; Li, H.; Barriga, F.J.A.S.; Liang, J.; Yang, W.; Yu, J.; Zhu, C. Bulk Geochemistry, Sulfur Isotope Characteristics of the Yuhuang-1 Hydrothermal Field on the Ultraslow-Spreading Southwest Indian Ridge. *Ore Geol. Rev.* **2018**, *96*, 13–27. [[CrossRef](#)]
46. He, C.; Ji, L.; Wu, Y.; Su, A.; Zhang, M. Characteristics of Hydrothermal Sedimentation Process in the Yanchang Formation, South Ordos Basin, China: Evidence from Element Geochemistry. *Sediment. Geol.* **2016**, *345*, 33–41. [[CrossRef](#)]
47. Mills, R.; Elderfield, H.; Thomson, J. A Dual Origin for the Hydrothermal Component in a Metalliferous Sediment Core from the Mid-Atlantic Ridge. *J. Geophys. Res.* **1993**, *98*, 9671. [[CrossRef](#)]
48. Mills, R.A.; Elderfield, H. Rare Earth Element Geochemistry of Hydrothermal Deposits from the Active TAG Mound, 26° N Mid-Atlantic Ridge. *Geochim. Cosmochim. Acta* **1995**, *59*, 3511–3524. [[CrossRef](#)]
49. Dutrieux, A.M. Rise and Fall of a Hydrothermal System: A Tale of Metalliferous Sediments (TAG Hydrothermal Field, MAR, 26°N). Ph.D. Thesis, University of Southampton, Southampton, UK, 2020.
50. Koschinsky, A.; Hein, J.R. Uptake of Elements from Seawater by Ferromanganese Crusts: Solid-Phase Associations and Seawater Speciation. *Mar. Geol.* **2003**, *198*, 331–351. [[CrossRef](#)]
51. Dubinin, A.V. Geochemistry of Rare Earth Elements in the Ocean. *Lithol. Miner. Resour.* **2004**, *39*, 289–307. [[CrossRef](#)]
52. Yu, Z.; Li, H.; Li, M.; Zhai, S. Hydrothermal Signature in the Axial-Sediments from the Carlsberg Ridge in the Northwest Indian Ocean. *J. Mar. Syst.* **2018**, *180*, 173–181. [[CrossRef](#)]
53. Nakamura, K.; Kato, Y.; Tamaki, K.; Ishii, T. Geochemistry of Hydrothermally Altered Basaltic Rocks from the Southwest Indian Ridge near the Rodriguez Triple Junction. *Mar. Geol.* **2007**, *239*, 125–141. [[CrossRef](#)]
54. Adachi, M.; Yamamoto, K.; Sugisaki, R. Hydrothermal Chert and Associated Siliceous Rocks from the Northern Pacific: Their Geological Significance as Indication of Ocean Ridge Activity. *Sediment. Geol.* **1986**, *47*, 125–148. [[CrossRef](#)]
55. Ding, T.; Wang, J.; Tao, C.; Dias, Á.A.; Liang, J.; Wang, Y.; Chen, J.; Wu, B.; Huang, H. Trace-Element Compositions of Sulfides from Inactive Tianzuo Hydrothermal Field, Southwest Indian Ridge: Implications for Ultramafic Rocks Hosting Mineralization. *Ore Geol. Rev.* **2021**, *140*, 104421. [[CrossRef](#)]
56. Tao, C.; Li, H.; Jin, X.; Zhou, J.; Wu, T.; He, Y.; Deng, X.; Gu, C.; Zhang, G.; Liu, W. Seafloor Hydrothermal Activity and Polymetallic Sulfide Exploration on the Southwest Indian Ridge. *Chinese Sci. Bull.* **2014**, *59*, 2266–2276. [[CrossRef](#)]
57. Chen, L.; Chu, F.Y.; Zhu, J.H.; Dong, Y.H.; Yu, X.; Li, Z.G.; Tang, L.M. Major and Trace Elements of Abyssal Peridotites: Evidence for Melt Refertilization beneath the Ultraslow-Spreading Southwest Indian Ridge (53° E Segment). *Int. Geol. Rev.* **2015**, *57*, 1715–1734. [[CrossRef](#)]
58. Schmidt, K.; Koschinsky, A.; Garbe-Schönberg, D.; de Carvalho, L.M.; Seifert, R. Geochemistry of Hydrothermal Fluids from the Ultramafic-Hosted Logatchev Hydrothermal Field, 15°N on the Mid-Atlantic Ridge: Temporal and Spatial Investigation. *Chem. Geol.* **2007**, *242*, 1–21. [[CrossRef](#)]
59. Mével, C. Serpentinization of Abyssal Peridotites at Mid-Ocean Ridges. *Comptes Rendus Geosci.* **2003**, *335*, 825–852. [[CrossRef](#)]
60. Sun, Z.; Cao, H.; Xijile, Y.; Zhang, X.; Dong, A.; Liu, L. Precipitation and Subsequent Preservation of Hydrothermal Fe-Mn Oxides in Distal Plume Sediments on Juan de Fuca Ridge. *J. Mar. Syst.* **2018**, *187*, 128–140. [[CrossRef](#)]
61. Fitzsimmons, J.N.; John, S.G.; Marsay, C.M.; Hoffman, C.L.; Nicholas, S.L.; Toner, B.M.; German, C.R.; Sherrell, R.M. Iron Persistence in a Distal Hydrothermal Plume Supported by Dissolved-Particulate Exchange. *Nat. Geosci.* **2017**, *10*, 195–201. [[CrossRef](#)]
62. Kennedy, C.B.; Scott, S.D.; Ferris, F.G. Hydrothermal Phase Stabilization of 2-Line Ferrihydrite by Bacteria. *Chem. Geol.* **2004**, *212*, 269–277. [[CrossRef](#)]
63. Mills, R.A.; Wells, D.M.; Roberts, S. Genesis of Ferromanganese Crusts from the TAG Hydrothermal Field. *Chem. Geol.* **2001**, *176*, 283–293. [[CrossRef](#)]
64. Dias, Á.S.; Barriga, F.J.A.S. Mineralogy and Geochemistry of Hydrothermal Sediments from the Serpentinite-Hosted Saldanha Hydrothermal Field (36° 34' N; 33° 26' W) at MAR. *Mar. Geol.* **2006**, *225*, 157–175. [[CrossRef](#)]
65. Edmonds, H.N.; German, C.R. Particle Geochemistry in the Rainbow Hydrothermal Plume, Mid-Atlantic Ridge. *Geochim. Cosmochim. Acta* **2004**, *68*, 759–772. [[CrossRef](#)]
66. Nagender Nath, B.; Balaram, V.; Sudhakar, M.; Plüger, W.L. Rare Earth Element Geochemistry of Ferromanganese Deposits from the Indian Ocean. *Mar. Chem.* **1992**, *38*, 185–208. [[CrossRef](#)]

67. Schwertmann, U.; Murad, E. Effect of PH on the Formation of Goethite and Hematite from Ferrihydrite. *Clays Clay Miner.* **1983**, *31*, 277–284. [[CrossRef](#)]
68. Fitzpatrick, R.W.; Roux, J.L.E.; Schwertmann, U. Amorphous and Crystalline Titanium and Iron-Titanium Oxides in Synthetic Preparations, At Near Ambient Conditions, and in Soil Clays. *Clays Clay Miner.* **1978**, *26*, 189–201. [[CrossRef](#)]
69. Zhao, J.; Huggins, F.E.; Zhen, F.; Huffman, G.P. Ferrihydrite: Surface Structure and Its Effects on Phase Transformation. *Clays Clay Miner.* **1994**, *42*, 737–746. [[CrossRef](#)]
70. Cornell, R.; Schwertmann, U. *The Iron Oxides: Structures, Properties, Reactions, Occurrences and Uses*; VCH Verlagsgesellschaft GMBH: Weinheim, Germany, 1996; pp. 533–559.
71. Ohmoto, H. Nonredox Transformations of Magnetite-Hematite in Hydrothermal Systems. *Econ. Geol.* **2003**, *98*, 157–161. [[CrossRef](#)]
72. Mehdipour Ghazi, J.; Harris, C.; Rahgoshay, M.; Moazzen, M. Combined Igneous and Hydrothermal Source for the Kiruna-Type Bafq Magnetite-Apatite Deposit in Central Iran; Trace Element and Oxygen Isotope Studies of Magnetite. *Ore Geol. Rev.* **2019**, *105*, 590–604. [[CrossRef](#)]
73. Knipping, J.L.; Bilenker, L.D.; Simon, A.C.; Reich, M.; Barra, F.; Deditius, A.P.; Wälle, M.; Heinrich, C.A.; Holtz, F.; Munizaga, R. Trace Elements in Magnetite from Massive Iron Oxide-Apatite Deposits Indicate a Combined Formation by Igneous and Magmatic-Hydrothermal Processes. *Geochim. Cosmochim. Acta* **2015**, *171*, 15–38. [[CrossRef](#)]
74. Simon, A.C.; Pettke, T.; Candela, P.A.; Piccoli, P.M.; Heinrich, C.A. Magnetite Solubility and Iron Transport in Magmatic-Hydrothermal Environments. *Geochim. Cosmochim. Acta* **2004**, *68*, 4905–4914. [[CrossRef](#)]
75. Dare, S.A.S.; Barnes, S.J.; Beaudoin, G.; Méric, J.; Boutroy, E.; Potvin-Doucet, C. Trace Elements in Magnetite as Petrogenetic Indicators. *Miner. Depos.* **2014**, *49*, 785–796. [[CrossRef](#)]
76. Cole, T.G. Composition, Oxygen Isotope Geochemistry and Origin of Smectite in the Metalliferous Sediments of the Bauer Deep, Southeast Pacific. *Geochim. Cosmochim. Acta* **1985**, *49*, 221–235. [[CrossRef](#)]
77. Cuadros, J.; Michalski, J.R.; Dekov, V.; Bishop, J.; Fiore, S.; Dyar, M.D. Crystal-Chemistry of Interstratified Mg/Fe-Clay Minerals from Seafloor Hydrothermal Sites. *Chem. Geol.* **2013**, *360–361*, 142–158. [[CrossRef](#)]
78. Surya Prakash, L.; John Kurian, P.; Resing, J.A.; Tsunogai, U.; Srinivas Rao, A.; Sen, K.; Lupton, J.E.; Baumberger, T.; Prajith, A.; Roy, P. Volatile-rich Hydrothermal Plumes over the Southern Central Indian Ridge, 24° 49' S: Evidence for a New Hydrothermal Field Hosted by Ultramafic Rocks. *Geochem. Geophys. Geosyst.* **2022**, *23*, e2022GC010452. [[CrossRef](#)]
79. Ray, D.; Kamesh Raju, K.A.; Baker, E.T.; Srinivas Rao, A.; Mudholkar, A.V.; Lupton, J.E.; Surya Prakash, L.; Gawas, R.B.; Vijaya Kumar, T. Hydrothermal Plumes over the Carlsberg Ridge, Indian Ocean. *Geochem. Geophys. Geosyst.* **2012**, *13*, 1–15. [[CrossRef](#)]
80. Qiu, Z.; Fan, W.; Han, X.; Chen, X.; Yin, X. Distribution, Speciation and Mobility of Metals in Sediments of the Tianxiu Hydrothermal Field, Carlsberg Ridge, Northwest Indian Ocean. *J. Mar. Syst.* **2023**, *237*, 103826. [[CrossRef](#)]
81. Mottl, M.J.; McConachy, T.F. Chemical Processes in Buoyant Hydrothermal Plumes on the East Pacific Rise near 21°N. *Geochim. Cosmochim. Acta* **1990**, *54*, 1911–1927. [[CrossRef](#)]
82. Rudnicki, M.D.; Elderfield, H. A Chemical Model of the Buoyant and Neutrally Buoyant Plume above the TAG Vent Field, 26 Degrees, N., Mid-Atlantic Ridge. *Geochim. Cosmochim. Acta* **1993**, *57*, 2939–2957. [[CrossRef](#)]
83. Leader, J.W.; Dunne, E.J.; Reddy, K.R. Phosphorus Sorbing Materials: Sorption Dynamics and Physicochemical Characteristics. *J. Environ. Qual.* **2008**, *37*, 174. [[CrossRef](#)]
84. Sands, C.M. Hydrothermal Plumes and Processes in the Indian Ocean. Ph. D. Thesis, School of Ocean & Earth Science, University of Southampton, Southampton, UK, 2006.
85. Feely, R.A.; Massoth, G.J.; Trefry, J.H.; Baker, E.T.; Paulson, A.J.; Lebon, G.T. Composition and Sedimentation of Hydrothermal Plume Particles from North Cleft Segment, Juan de Fuca Ridge. *J. Geophys. Res. Solid Earth* **1994**, *99*, 4985–5006. [[CrossRef](#)]
86. Gartman, A.; Findlay, A.J.; Luther, G.W. Nanoparticulate Pyrite and Other Nanoparticles Are a Widespread Component of Hydrothermal Vent Black Smoker Emissions. *Chem. Geol.* **2014**, *366*, 32–41. [[CrossRef](#)]

Disclaimer/Publisher's Note: The statements, opinions and data contained in all publications are solely those of the individual author(s) and contributor(s) and not of MDPI and/or the editor(s). MDPI and/or the editor(s) disclaim responsibility for any injury to people or property resulting from any ideas, methods, instructions or products referred to in the content.